Quantitative diffuse optical spectroscopy for noninvasive measurements of the malaria pigment hemozoin

CHRIS CAMPBELL AND THOMAS D. O'SULLIVAN[*] ⓘD

Department of Electrical Engineering, University of Notre Dame, 275 Fitzpatrick Hall of Engineering, Notre Dame, IN 46556, USA
[*]*tosullivan@nd.edu*
https://osullivangroup.nd.edu/

Abstract: Hemozoin (Hz) is a crystal by-product of hemoglobin consumption by malaria parasites. There are currently no *in vivo* deep tissue sensing methods that can quantify Hz presence noninvasively, which would be advantageous for malaria research and treatment. In this work, we describe the broadband near-infrared optical characterization of synthetic Hz in static and dynamic tissue-simulating phantoms. Using hybrid frequency domain and continuous-wave near-infrared spectroscopy, we quantified the broadband optical absorption and scattering spectra of Hz and identified the presence of Hz at a minimum tissue-equivalent concentration of 0.014 μg/mL in static lipid emulsion phantoms simulating human adipose. We then constructed a whole blood-containing tissue-simulating phantom and demonstrated the detection of Hz at physiologically-relevant tissue oxygen saturations ranging from 70-90%. Our results suggest that quantitative diffuse optical spectroscopy may be useful for detecting deep tissue Hz *in vivo*.

1. Introduction

Malaria claims almost half a million lives worldwide every year and sickens millions more [1]. Efforts to eradicate the disease are under development, from new drugs and vaccines to techniques that reduce or eliminate its transmission vectors [2,3]. These efforts can benefit from noninvasive *in vivo* imaging tools that provide quantitative measures of malaria infection and its effect on specific tissue locations, monitor disease progression, and evaluate response to treatment.

Diffuse optical spectroscopy (DOS) is a noninvasive sensing and imaging technique which uses visible and near-infrared (NIR) light to characterize optical absorbers from deep (up to 2-3 cm) tissue including water, oxy- and deoxyhemoglobin, myoglobins, lipids, and melanin. By assessing absolute and changing concentrations of these chromophores, DOS technology shows promise for many clinical applications including functional brain imaging [4], monitoring neoadjuvant chemotherapy in breast cancer [5], quantifying blood perfusion in diabetic patients with peripheral arterial disease [6], and assessing the severity of burns and health of skin grafts in burn patients [7]. In addition to the stronger optical absorbers mentioned, tissue includes numerous minor absorbers in small concentrations that can be of great physiological significance. These include, for example, cytochrome c oxidase [8], dyshemoglobins (e.g., methemoglobin (MetHb), carboxyhemoglobin) [9], and the subject of this manuscript, hemozoin (Hz) [10].

Hz crystals are synthesized in red blood cells (RBCs) that are infected by malaria parasites, particularly the deadly species *p. falciparum*. As the maturing parasite consumes hemoglobin from the host RBC, toxic heme molecules are rendered safe through reorganization into Hz crystals [10]. To escape filtration by the spleen, mature, Hz-bearing parasites sequester in small blood vessels throughout the body by causing the host RBC to adhere to the vascular endothelium [11]. In addition to major organs including the brain, sequestered parasites are also found in adipose tissue [12]. There currently is not a suitable noninvasive deep tissue imaging technique

available to quantify and map the tissue distribution of infected RBCs *in vivo*; current methods to assess distribution in humans are completed postmortem [13]. If it were possible, accurate noninvasive measurements of the distribution and concentration of Hz *in vivo* could provide valuable insight into the development of Hz-based diagnostics, as well as improve understanding, monitoring, and treatment of severe complications of malaria such as cerebral malaria.

Hz exhibits measurable visible absorption in the 600-700 nm range and birefringence that has been detected via optical interrogation methods without requiring blood draws or dissection [14,15]. In this study, we hypothesized that Hz's unique optical absorption signature is detectable with DOS at concentrations relevant for monitoring malaria infection *in vivo*. If true, DOS could provide a quantitative, noninvasive *in vivo* measurement of deep tissue Hz that reflects the concentration of sequestered and circulating infected RBCs. To that end, we first measured the scatter-corrected absorption spectrum of Hz in a liquid, lipid emulsion, tissue-simulating phantom. Then, we constructed more complex phantoms containing whole blood and Hz to assess the ability of DOS to noninvasively measure Hz concentrations in adipose tissue over a physiological range of tissue oxygen saturation. Our data suggest that noninvasive DOS is indeed sensitive to clinically-relevant concentrations of Hz in adipose-like tissue and capable of identifying its presence over a range of tissue oxygen saturation, although further work can be done to improve sensitivity and accuracy. To our knowledge, this work is the first to evaluate the potential of DOS for quantifying Hz in a noninvasive manner.

2. Methods

2.1. Quantitative broadband DOS technique

We used quantitative broadband DOS to characterize Hz-containing solutions and tissue-simulating phantoms. This technique, based on the design by Bevilacqua et al. [16], combines frequency-domain (FD) interrogation with laser diodes at discrete wavelengths, and broadband continuous-wave (CW) DOS, to measure absolute optical absorption and reduced scattering from 600 to 1000 nm. The experimental system is sketched in Fig. 1. Measurements of liquid tissue-simulating phantoms were performed using a reflectance geometry because preliminary Monte Carlo simulations [17] (not shown) revealed that inserting the large hybrid FD/CW fiber ferrules into the medium would violate an infinite boundary condition to the diffusion approximation and appreciably affect optical property estimation.
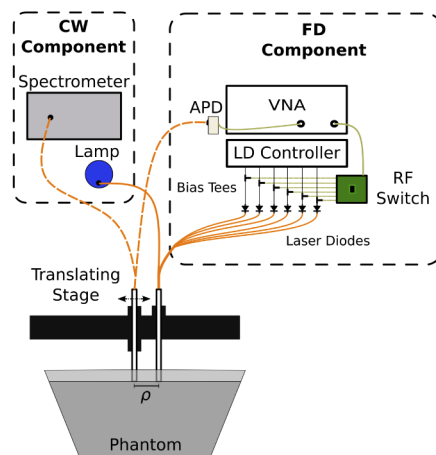

Fig. 1. Schematic of the FD/CW-DOS multi-distance system used in this study.

2.2. System components

2.2.1. Multi-frequency FD-DOS system

The FD-DOS portion of the system, described previously [18], consists of a vector network analyzer (VNA) (Agilent 8753ES), laser driver (Newport/ILX Lightwave LDC-3908), and an 8x1 integrated circuit based RF switch to sequentially intensity-modulate the six laser diodes (631, 660, 689, 782, 828, and 849 nm). The detector is an avalanche photodiode (APD) module (Hamamatsu C5658) modified with a 1mm circular APD (Hamamatsu S12060-10). Average optical power was set to 25 mW when each laser was energized.

Early data was acquired with 17 source-detector separations (SDS) from 14 to 30 mm, and measured at 401 frequencies from 10-560 MHz. Later experiments were optimized to measure at only 4 SDS (11, 12, 17, and 18 mm) while reducing the input frequency bandwidth on the VNA, which had a similar beneficial effect on the signal-to-noise ratio (SNR) and measurement accuracy. These optimized measurements used 201 frequencies from 20-460 MHz.

2.2.2. Broadband CW-DOS system

Broadband CW measurements were performed at an SDS 1 mm shorter than each FD measurement, due to the position of the broadband detector in the fiber probe. A tungsten-halogen light source (Ocean Optics HL-2000-FHSA) and a high-throughput visible-NIR spectrometer (Avantes HS2048XL-EVO) were used. To ensure that broadband reflectance (i.e., spectrometer counts) measured across the entire spectrum fell within the linear dynamic range of the spectrometer, we first optimized the integration time at each SDS so peak counts registered between 80 and 90% of the spectrometer bit depth (2^{16} counts). When needed, to increase the signal in ranges with high absorption (i.e., low counts), we doubled the integration time and stitched the two dark-subtracted intensity curves (corrected for integration time) together. We confirmed that saturated pixels did not negatively affect other pixels registering within their linear dynamic range. With this technique, most pixels recorded data in the linear range; those that did not were discarded.

2.2.3. Optical fiber probe and stage

Seven 400 μm low-OH, silica-silica fibers arranged in a 6-on-1 hexagonal configuration delivered light to the phantom. Remitted light was collected with two 1 mm solid-core fibers (one each for broadband and FD). The FD detector fiber (NA 0.48, hard-clad silica) was coupled to the APD module using a matched pair of lenses. Broadband CW illumination was delivered via the central 400 μm source fiber and collected with the second detector fiber (NA 0.22, silica-silica). The source and detector fibers were bundled together in two 6.4 mm diameter stainless steel ferrules. The distance between the two ferrules was adjusted with a translating stage (Thorlabs LTS300).

2.3. Measurement processing

All experiments were accomplished in a self-calibrated fashion using a multi-distance approach to avoid the reliance on calibration standards. We chose this approach for two reasons. First, calibration standards for diffuse optical measurements are generally not traceable, and error in the characterization of these calibration standards could be quite large [19] and will induce roughly equal (percentage-wise) error into measured optical properties. Second, most calibration phantoms are made of a solid material (e.g., silicone), while the present study was performed in liquid phantoms. Our initial experiments demonstrated that differences in optical coupling between the fiber probes and the solid calibration vs liquid Hz phantoms were resulting in inaccuracies in the optical property estimation. Since consistent multi-distance optical coupling is more easily achieved in a liquid phantom, liquid phantoms offer the beneficial opportunity to make highly accurate self-calibrated measurements. Because the data acquisition speed

of the multi-distance approach is relatively slow (ten minutes for a full measurement), time-sensitive blood phantom measurements were necessarily performed at a single SDS. Single SDS measurements were calibrated to a multi-distance measurement acquired from the same solution under static conditions at the conclusion of the experiment, negating the need for a separate calibration phantom.

Multi-distance, multi-frequency, multi-wavelength FD-DOS provides a robust and complex dataset that can improve optical property and chromophore accuracy. However, intelligent data filtering is necessary since including data with low SNR (e.g., at higher modulation frequencies and long SDS) can undercut this benefit. Therefore, data that failed to meet SNR criteria were discarded. These criteria and the pairwise fitting procedure for FD and CW measurements are described below.

2.3.1. FD processing

The FD component of the system captured intensity-modulated data, which was then fit to an analytical semi-infinite P1 approximation of the radiative transport equation model to estimate optical properties [20,21]. Multi-distance FD reflectance data were utilized in the model pairwise (e.g., the complex-valued ratio of 17 mm SDS reflectance with 11 mm SDS). A representative multi-distance measurement and its model fit are shown in Fig. 2. Since we used a point-source approximation to model optical fibers with finite numerical apertures, we found that comparing a pair of measurements less than 10 fiber diameters apart could introduce non-negligible error. As a result, ratios were only compared for SDS pairs separated by 5 mm or more.
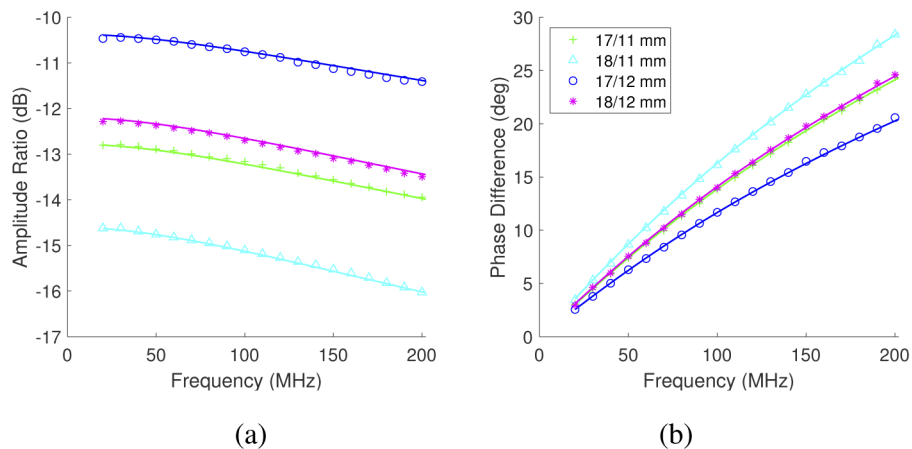

Fig. 2. Representative self-calibrated multi-distance FD-DOS data and the accompanying model fit at 660 nm. The medium is an Intralipid phantom with 1 μg/mL Hz. The modulation frequency cutoff (202 MHz) was chosen in combination with the maximum SDS (18 mm) to ensure all data were above the noise floor. Each line represents a comparison of the measurements at two source-detector separations: ratio of amplitude (a) and difference in phase (b). The markers represent every fifth frequency measured.

The FD noise floor was determined by acquiring dark measurements after each experiment, wherein the source and detector fibers were optically blocked. The SNR criterion was chosen to be 10 dB above the mean dark amplitude (i.e., noise floor) for each modulation frequency and wavelength. A modulation frequency cut-off was chosen as the first of three sequential frequencies that failed to meet the SNR requirement. This limit informed the choice of maximum SDS to include in the fit, and the lowest cut-off frequency selected was applied to all selected SDS for ease of fitting. The maximum SDS choice reflected a compromise between frequency

content and number of SDS, though the final cutoff (+/- 1 mm) did not have a significant effect on the measurement accuracy, given all the included data was above the noise floor.

2.3.2.   CW processing

Accurately measuring both absorption and scattering from a single series of CW reflectance measurements is difficult, if not impossible, even with minimal experimental noise present. Therefore, the broadband scattering spectrum estimated from the power law fit of the discrete (multi-distance) FD-DOS optical scattering coefficients [22] was used to constrain a multi-distance CW reflectance model and estimate broadband absorption. Then we compared the measured broadband absorption spectra to the discrete wavelength FD-DOS derived absorption coefficients for confirmation. Misfits between FD and CW components could indicate a problem with the experiment or data processing and provide a rough estimate of the experimental uncertainty. An example CW reflectance dataset with accompanying fit is shown in Fig. 3, while the typical agreement of the FD- and CW-DOS derived optical properties are shown in Fig. 4(a).
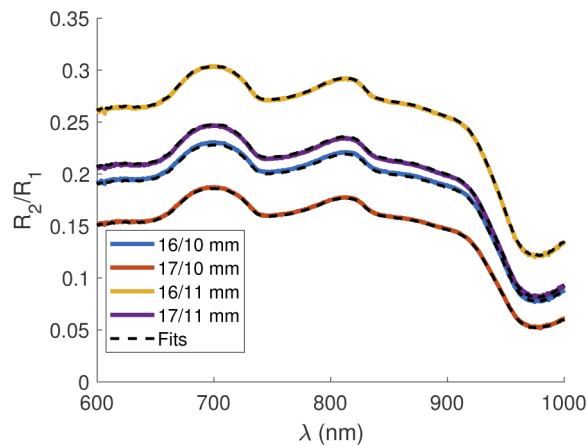

Fig. 3. Representative self-calibrated multi-distance broadband CW reflectance data and model fit, with μ'_S constrained by the frequency domain power law fit. The medium is an Intralipid phantom with 1 μg/mL Hz.

2.3.3.   Chromophore estimation

For the bovine blood phantoms, we initially fit four basis spectra: bovine oxyhemoglobin (HbO$_2$), bovine deoxyhemoglobin (HHb) [9], and water all from literature values, as well as the experimentally-derived Hz. As work progressed, it became apparent that the absorption spectrum of water was not matching the absorption of the (mostly-water) Intralipid component. Specifically, the water absorption peak and width was slightly different than the experimental data, which is expected due to variations in temperature and protein binding [23,24] (even after correcting for the lipid component). Therefore we separately measured the absorption spectrum for Intralipid and water mixed at a 1% concentration with the multi-distance approach and used this as the basis chromophore for Intralipid+water in the blood phantom. Total Hemoglobin concentration (THb) was calculated by adding HbO$_2$ and HHb. The basis spectra components are shown in Fig. 4(b).

Figure 4(a) demonstrates the results of a typical broadband fit. The mean difference between the fitted chromophore absorption and measured broadband absorption is 1.4×10^{-4} mm^{-1} (1.7%), and the mean difference between FD and CW absorption is 2.4×10^{-4} mm^{-1} (3.5%).
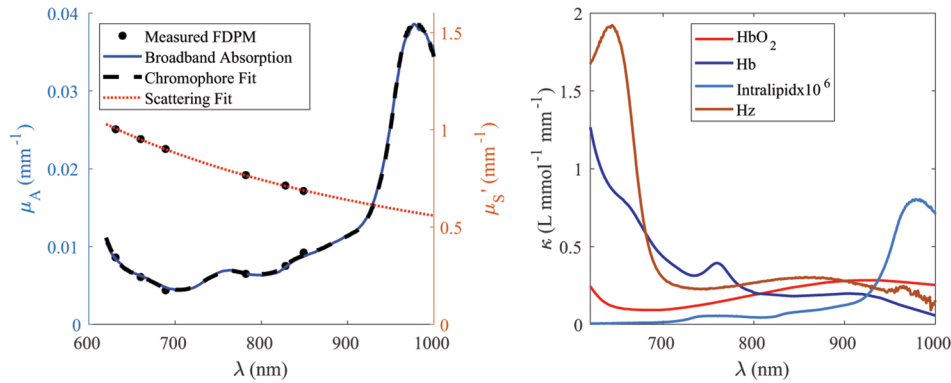
Fig. 4. (a) Absorption and reduced scattering spectrum obtained with quantitative broadband DOS, of a bovine blood phantom at 80% saturation. Scattering was estimated via a power-law fit to the FD-DOS coefficients. Broadband reflectance was calibrated with the reconstructed broadband system response from a multi-distance fit. (b) Individual chromophore spectra

2.4. Phantom construction

Liquid phantoms were selected for this study because they allow for dynamic adjustment of their optical properties. The phantoms were constructed in a cylindrical vessel with a 20 cm diameter to minimize boundary reflections and continuously stirred with a stir bar during experiments to maintain homogeneity. The stir speed was chosen to minimize vortex size while also disrupting the propagation of surface waves. For this configuration, the stir speed was 100 rpm.

Since the phantom experiments required several hours to conduct, we observed that evaporation could affect optical coupling at the liquid surface. To counter this, a custom lid was fabricated with black, open-cell foam to cover the phantom mixture and minimize reflection. Holes in the lid permitted the insertion and translation of the fiber ferrules, as well as the insertion of a dissolved oxygen (DO) sensor (Hamilton, P/N 243666-121).

Three phantom types were constructed for this work: a static Hz+Intralipid phantom for measuring the optical properties of Hz, and dynamic Hz+Intralipid+blood and Intralipid+blood (i.e., control) phantoms for simulating tissue at varying levels of oxygenation. Table 1 details the composition of each phantom type.

Table 1. Phantom ingredients

Phantom	PBS 1X(mL)	20% Intralipid(mL)	Nigrosin(nmol)	Hz(mg)	Blood/Citrate(mL)
Hz+Intralipid	1900	100	150	0 - 38	-
Hz+Intralipid+blood	2270	110	-	0.325	37
Intralipid+blood (control)	2270	110	-	-	37

2.4.1. Hz absorption phantom

A phantom designed for accurately measuring the absorption spectrum of Hz in Intralipid was constructed from deionized (DI) water and lipid emulsion (Fresenius Kabi AB, Intralipid 20%). Nigrosin (Sigma Aldrich 198285) was also added to assure a nonzero baseline absorption. The baseline absorption spectrum for this Hz-free phantom was acquired using three multi-distance measurements. Synthetic Hz (Invivogen, tlrl-hz) was then dispersed in DI water and added to the phantom mixture in 1 mL aliquots (approximately 200 μg Hz) between measurements. After measuring the absorption of the phantom at each concentration with a multi-distance

measurement, we performed a linear regression to estimate the absorption spectrum of Hz ($\mu_{A,Hz}$) using the formula

$$\mu_A(\lambda) = \mu_{A,baseline}(\lambda) + [c] * \mu_{A,Hz}(\lambda), \tag{1}$$

where μ_A is the measured Hz phantom absorption spectrum, $\mu_{A,baseline}(\lambda)$ is the measured Hz-free phantom absorption spectrum, and $[c]$ is the concentration of Hz. The concentration of Hz was calculated according to the molecular weight of a Hz dimer (1228.9495 g/mol) [10].

2.4.2. Blood oxygenation phantom with Hz

Another Intralipid-based phantom simulating human adipose tissue with a blood volume fraction (BVF) of 1% was constructed to assess the ability of quantitative broadband DOS to noninvasively quantify Hz at varying tissue oxygen saturation [25]. Potential interference with HHb, which exhibits significant absorption in the same spectral region, was of particular interest. We began with a 2.3 L bath of 1x phosphate-buffered saline (PBS) to prevent the rupturing of red blood cells due to osmotic pressure. To this bath, we added 100 mL Intralipid 20%. We used fresh, whole bovine blood because its properties are similar to human blood, with one relevant exception. Bovine blood reference values for hematocrit and mean corpuscular hemoglobin are both lower than those for human blood. To compensate for this, we used 1.3 times the blood required for a 1% human BVF [26,27]. All phantoms were kept at room temperature, rather than body temperature, to limit evaporation. In blood phantoms, lower-than-physiological temperature increases the oxygen affinity of the blood but should not otherwise change its optical absorption or interaction with other phantom ingredients. To simulate moderate *p. falciparum* malaria infection of 0.5% parasitemia (16 μg/mL of blood, or 0.16 μg/mL of tissue), [28], we added 375 μg Hz to the phantom.

The blood phantom was deoxygenated by bubbling nitrogen gas through the initial Intralipid and PBS mixture until DO measured less than 5% of its equilibrium value. Then we stopped the gas flow and added 37 mL of fresh, whole bovine blood (with anticoagulant). We elected to use this approach over introducing yeast or sodium dithionite to deoxygenate because the simple chemistry should not affect the phantom optical properties other than altering hemoglobin state.

The blood was collected fresh, at most five hours prior to the start of the experiment, and mixed well with citrate (Sigma Aldrich S5770) anticoagulant in a 9-to-1 ratio by volume. The containers of blood/citrate mix were immediately placed on ice for transport, and stored in a refrigerator at the destination at 4° C. Optical measurements were collected every 30 seconds during reoxygenation. Following the conclusion of the Hz-blood deoxygenation experiment, a control blood phantom with no Hz was mixed using the remaining blood (now approximately ten hours old).

3. Results

3.1. Hz absorption spectrum

Absorption spectra for Hz suspended in an Intralipid/nigrosin solution at concentrations ranging from 0.01 to 9.2 μg/L are shown in Fig. 5(a). Unlike previously published attenuation spectra for synthetic Hz [29,30], these spectra are corrected for optical scattering that occurs when the solid crystals are suspended in solution. From these data, the slope of a least-squares linear fit to absorption as a function of Hz concentration at each wavelength (e.g., Fig. 6) yields the broadband absorption spectrum (Fig. 5(b)). Uncertainty increases near the 978 nm water peak, where the albedo and spectrometer sensitivity are reduced. Additionally, the Hz peak in Intralipid solution was measured to be at 643 nm, 22 nm shorter than previously reported [29,30], and confirmed with spectrophotometry (Jasco V-760, data overlaid in Fig. 5(b)). This implies that there are solvatochromic interactions with the Intralipid that alter the absorption spectrum. We identified the presence of Hz absorption at all measured concentrations in this phantom.
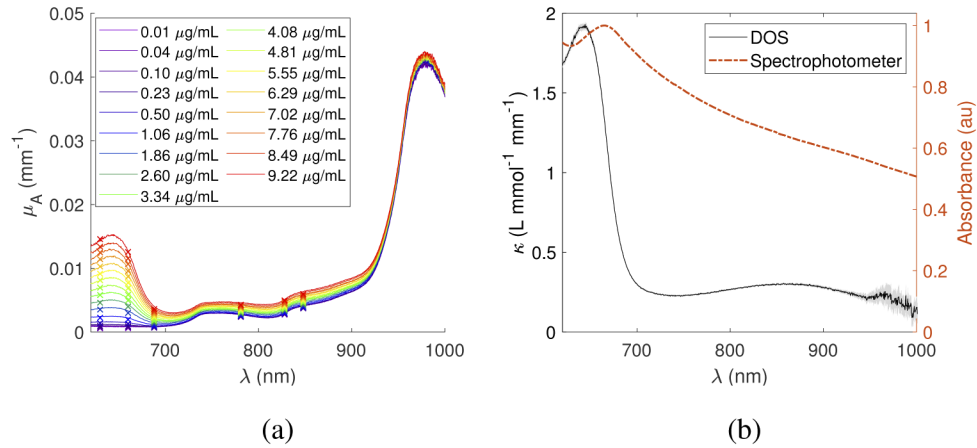
Fig. 5. (a) Absorption spectra for increasing concentrations of Hz. (b) Measured molar absorption spectrum for Hz, overlaid with attenuation spectrum of Hz in DI water. The shaded uncertainty region represents the interquartile range of the normalized difference between absorption spectra and their fits.
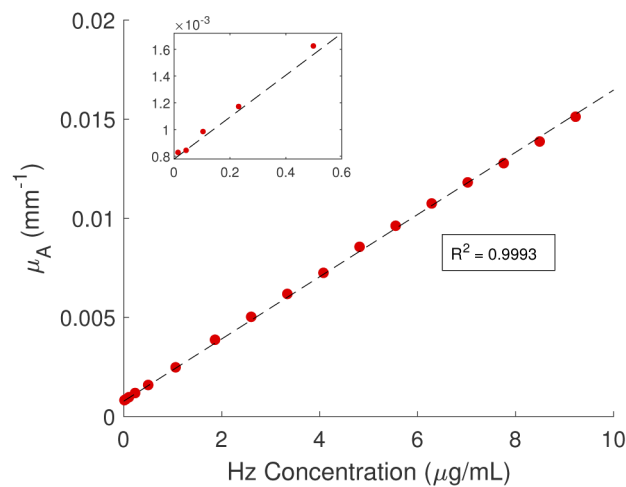

Fig. 6. Measured absorption of Hz at 643 nm with increasing concentration.

We utilized a separate set of Hz+Intralipid phantom data to assess the accuracy of quantifying Hz concentrations using the derived Hz molar absorption spectrum. Figure 7 shows the Hz concentrations estimated from the absorption spectra measured in these phantoms, compared to the added amount. We conclude that we can quantify differences in Hz concentrations in a phantom down to approximately 0.12 µg/mL. Though recovered concentrations are approximately linear with the amount added, the slope is shallower compared to the ideal relationship. Intense sonication and repeated rinsing of the syringe vials the Hz was packaged in did not always succeed in extracting all of the crystals. A fraction left in the vials when preparing the subsequent Hz absorption phantoms could have led to an underestimation. In addition, the non-zero y-intercept suggests that some measured Hz may be due to crosstalk with another phantom component or error introduced by measurement uncertainty (i.e., low SNR).
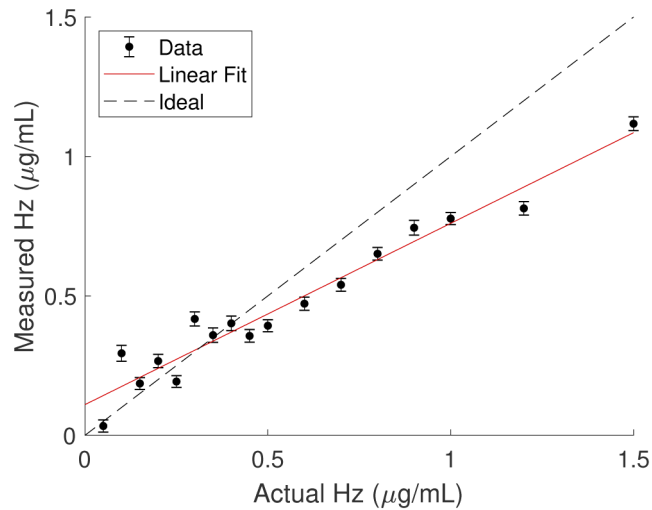

Fig. 7. Measured concentrations of Hz in Intralipid phantoms, using the absorption spectrum in Fig. 5(b). Error bars represent +/- 2 standard error of the chromophore concentration estimated from the linear regression of the Hz absorption spectrum to the measured absorption spectrum.

3.2. Blood-Intralipid phantoms

Hz absorption in liquid phantoms containing whole bovine blood under varying oxygen saturation were measured to simulate more optically challenging and realistic physiological conditions. Oxygenation was increased under ambient air from near zero to 100% blood oxygen saturation in two phantoms: with and without Hz. Measured HbO_2, HHb, THb, as well as oxygen saturation from both the Hz-containing and non-Hz control phantoms are plotted against the measured DO in Fig. 8(a). The control experiment, with no Hz, is represented by open circles. As expected, the hemodynamic profiles match between the Hz and control phantom. The control phantom shows slightly higher total hemoglobin; we attribute this to measurement errors arising when the blood was mixed with anticoagulant, and when it was dispensed. The slight discontinuities in THb (e.g., at 13, 15, 18, 20, 23, 27. and 31% DO for the Hz containing phantom) coincide with time points when 2.5 mL (0.1% of the phantom volume) of DI water was added to counteract evaporation of the aqueous phantom. Further, oxygen saturation (StO_2) increases as expected with increasing dissolved oxygen.

Finally, we present the recovered Hz from both the Hz and control phantoms. The measured Hz concentration for each phantom is plotted in Fig. 9. As expected, the values for the phantom
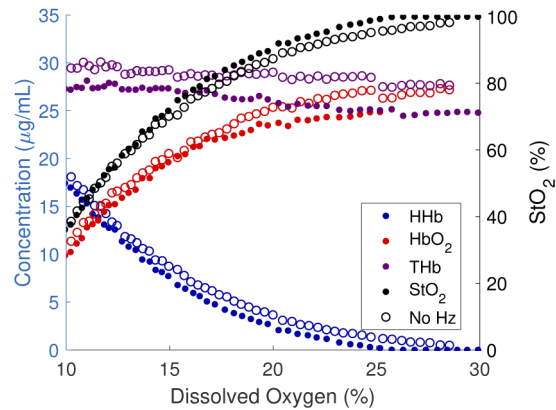
Fig. 8. HbO_2, HHb, and THb measurements versus DO, and the reconstructed HbO_2 dissociation curves for each experiment. Closed circles represent the experiment containing Hz, while open circles represent the control.

containing Hz were significantly higher than for the control, but they were overestimated in both phantoms (i.e., should be zero in the control). This is similar to the offset observed at the similar low concentration in Fig. 7. A possible reason for this overestimation is crosstalk with HHb given the spectral overlap below 700 nm, and further investigation is needed.
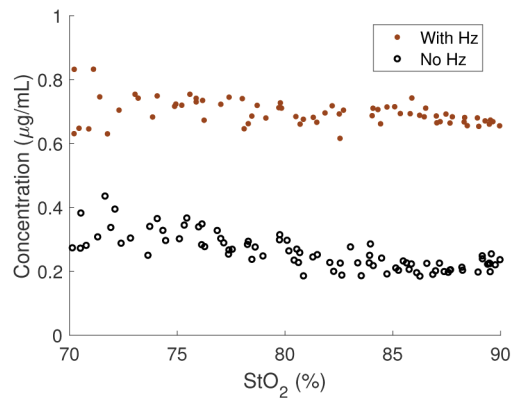

Fig. 9. Measured Hz concentration as a function of measured oxygen saturation between 70 and 90%.

4. Discussion

The goal of this work was to assess whether deep tissue DOS could be used to quantify clinically and preclinically-relevant concentrations of Hz *in vivo*. There exist few imaging techniques sensitive to Hz *in vivo* such as multi-modal magneto-optical [31] and photoacoustic [32] approaches. While these techniques have excellent sensitivity that are similar to or better than rapid diagnostic tests, their field of view is limited to shallow or single vessels. DOS, on the other hand, probes a much larger tissue volume and depth, while closely related techniques such as spatial frequency domain imaging [33] can rapidly image wide fields of view.

A deep tissue imaging approach could provide researchers an important tool for studying the pattern of infected red blood cell sequestration, elucidating the ligands and host tissue receptors responsible for this process, as well as the relationship between clinical symptoms and the

underlying causes. This need is especially significant for better understanding cerebral malaria, which is a severe and oftentimes fatal syndrome resulting from severe malaria and is associated with seizures, retinopathy, brain swelling, and coma. Sequestration has been hypothesized as having an important role in the pathogenesis of cerebral malaria, although the exact mechanisms are still unclear [34]. Currently, the primary approach to assess sequestration in humans is through postmortem examination, making it very difficult to correlate with clinical symptoms.

Furthermore, disruption of Hz production is a major target for malaria therapeutics, including what was formerly the best drug for malaria treatment, chloroquine. Because of widespread resistance to chloroquine, there have been renewed efforts to develop new therapeutics that also disrupt the Hz pathway and lead to the accumulation of toxic heme in the infected host cells resulting in cell death. Noninvasive *in vivo* Hz sensing and imaging could serve as a useful preclinical tool for assessing new drugs and targets as well as characterizing treatment response by measuring and mapping where infected RBCs have been cleared. Since Hz induces and disrupts the host immune response, a DOS-based technique could provide a simple approach to image the tissue distribution of Hz together with markers of immune response (e.g., oxyhemgoglobin) longitudinally *in vivo*.

With these long-term goals in mind, the necessary first step in this line of research was to measure the near-infrared absorption spectrum of synthetic Hz suspended in a tissue-simulating lipid emulsion phantom. This was necessary because, to our knowledge, the only reported Hz spectra were of its absorbance that includes both attenuation due to absorption and scattering from the Hz crystals. The self-calibrated multi-distance quantitative broadband DOS technique employed here is ideal because it decouples the effects of the optical absorption and scattering and does not rely on the accurate a priori characterization of a calibration phantom. During this experiment, we observed absorption contrast to Hz even at the lowest measured concentration of 0.014 µg/mL. The absorption contribution at peak Hz absorption was 0.0008 mm^{-1}, which is similar to the precision of a deep tissue DOS measurement [18].

After this data was used to reveal the Hz (in Intralipid) extinction spectrum, we quantified Hz in a subsequent phantom with a sensitivity of approximately 0.12 µg/mL. We then demonstrated Hz detection in a whole blood-based phantom simulating human adipose tissue with an adipose tissue Hz concentration of 0.16 µg/mL (i.e., 0.5% parasitemia or 16 µg/mL in blood corresponding to a moderate malaria infection, discussed below) through a physiological range of tissue oxygen saturations. Because Hz was overestimated in both the Hz+blood phantom and the blood-only control phantom, there may have been crosstalk interference with HHb, which will be the subject of a future investigation.

To our knowledge, this is the first time that a quantitative DOS technique has been used to measure Hz. A natural question to ask is: given our results, how sensitive can DOS be for either diagnostics or characterization of disease progression and treatment response? One indicator of the severity of a malaria infection is parasitemia, which can be estimated from thin blood smears as the number of parasites expected per volume of blood. The sensitivity limit of microscopy is as low as 4 parasites/µL, with low-level parasitemia at <100 parasites/µL and severe malaria found with >250,000 parasites/µL [28,35,36]. The level of parasitemia at which clinical symptoms (e.g., fever) appear varies greatly depending upon immune response, which is dependent upon age, geography and seasonal exposure, and other factors. For example, it has been shown that an appropriate cut-off value indicating clinical malaria in older children in an endemic area of Kenya is 2,500 parasites/µL [37].

However, the amount of Hz expected to present in tissue is not related to parasitemia in a simple manner because the amount of Hz present inside infected cells also depends upon the development stage of the parasite itself and the tissue distribution of the infected cells. Infected RBCs express proteins which cause sequestration of infected cells to the endothelial cells of the microvasculature and vary by tissue location and organ. This means Hz is not evenly distributed

in the body; common sites discovered upon post mortem examination include, for example, cerebral cortex, intestine, skin, lungs, and adipose tissue [13]. Because of the complexity in establishing a relevant threshold for Hz detection, we adopted the approach utilized by Newman et al. 2008 [28] to estimate the concentration of Hz present in the tissue for a given level of parasitemia (i.e., 100 parasites/μL corresponds to 0.06 μg/mL in whole blood). The lowest observed concentration of Hz in the Intralipid phantom experiment (which was diluted to simulate the Hz concentration in 1% BVF adipose tissue) thus corresponds to a parasitemia (2,300 parasites/μL) close to the threshold observed for clinical malaria symptoms in older children in endemic areas. The Hz concentration we chose for the blood phantoms was 12x higher because we expected reduced sensitivity due to the high absorption of hemoglobin in the same wavelength range, and corresponds to the level of a moderate malaria infection (27,000 parasites/μL). Given the data, we conclude that deep tissue noninvasive DOS as performed in this work may already be sensitive to moderate to malaria infections *in vivo*, but further improvements are necessary for DOS to be useful as an early diagnostic.

Our work revealed an unexpected finding that warrants further investigation as this research progresses toward *in vivo* applications. The Hz absorption peak in Intralipid solution was unexpectedly measured to be at 643 nm, approximately 22 nm shorter than previously reported [29,30]. We believe that this could be due to a chemical interaction with Intralipid as we observed the wavelength shift scaled with Intralipid concentration up to approximately 0.25%. Therefore, more work is needed to understand these effects and perhaps find a dispersion medium that scatters light without perturbing the absorption spectra of Hz in tissue. If the Hz absorption peak truly is closer to the 665 nm peak *in vivo*, we expect that the sensitivity of the technique will increase because of reduced spectral overlap with the absorption of HHb. Indeed this DOS technique could help reveal the actual *in vivo* Hz absorption spectrum during the first set of *in vivo* experiments. Once the *in vivo* absorption spectrum is well-characterized, we believe that DOS imaging of preclinical models of malaria could be a viable approach to quantify and map Hz distribution at different levels of parasitemia. We also anticipate that further improvements in sensitivity can be achieved by using a spectrometer with higher sensitivity in the red spectral region where Hz and hemoglobin absorption is significant.

5. Conclusion

In summary, we have demonstrated measurements of Hz in static and dynamic tissue-simulating phantoms as an important first step towards noninvasive *in vivo* sensing of malaria infection using DOS. We have identified challenges to noninvasive Hz sensing using broadband quantitative DOS and proposed methods to further improve sensitivity and accuracy. With further development and validation, noninvasive deep tissue Hz *in vivo* sensing and imaging could prove to be a useful tool for studying malaria infection and, ultimately, monitor disease progression and response.

Disclosures

TDO discloses patents related to FD-DOS technology and ownership of NearWave, Inc, which is producing a commercial FD-DOS device.

TDO: NearWave, Inc. (I, E, P)

References

1. "World malaria report 2019," Library Catalog: www.who.int.

2. R. E. Cibulskis, P. Alonso, J. Aponte, M. Aregawi, A. Barrette, L. Bergeron, C. A. Fergus, T. Knox, M. Lynch, E. Patouillard, S. Schwarte, S. Stewart, and R. Williams, "Malaria: Global progress 2000 - 2015 and future challenges," Infect. Dis. Poverty **5**(1), 61 (2016).

3. B. F. Hall and A. S. Fauci, "Malaria Control, Elimination, and Eradication: The Role of the Evolving Biomedical Research Agenda," J. Infect. Dis. **200**(11), 1639–1643 (2009). Publisher: Oxford Academic.

4. D. A. Boas, C. E. Elwell, M. Ferrari, and G. Taga, "Twenty years of functional near-infrared spectroscopy: introduction for the special issue," NeuroImage **85**, 1–5 (2014).

5. B. J. Tromberg, Z. Zhang, A. Leproux, T. D. O'Sullivan, A. E. Cerussi, P. M. Carpenter, R. S. Mehta, D. Roblyer, W. Yang, K. D. Paulsen, B. W. Pogue, S. Jiang, P. A. Kaufman, A. G. Yodh, S. H. Chung, M. Schnall, B. S. Snyder, N. Hylton, D. A. Boas, S. A. Carp, S. J. Isakoff, and D. Mankoff, "Predicting Responses to Neoadjuvant Chemotherapy in Breast Cancer: ACRIN 6691 Trial of Diffuse Optical Spectroscopic Imaging," Cancer Res. **76**(20), 5933–5944 (2016).

6. C. Weinkauf, A. Mazhar, K. Vaishnav, A. A. Hamadani, D. J. Cuccia, and D. G. Armstrong, "Near-instant noninvasive optical imaging of tissue perfusion for vascular assessment," J. Vasc. Surg. **69**(2), 555–562 (2019).

7. G. T. Kennedy, R. Stone, A. C. Kowalczewski, R. A. Rowland, J. H. Chen, M. L. Baldado, A. Ponticorvo, N. P. Bernal, R. J. Christy, and A. J. Durkin, "Spatial frequency domain imaging: a quantitative, noninvasive tool for *in vivo* monitoring of burn wound and skin graft healing," J. Biomed. Opt. **24**(7), 1–9 (2019).

8. M. G. Mason, P. Nicholls, and C. E. Cooper, "Re-evaluation of the near infrared spectra of mitochondrial cytochrome c oxidase: Implications for non invasive in vivo monitoring of tissues," Biochim. Biophys. Acta, Bioenerg. **1837**(11), 1882–1891 (2014).

9. W. G. Zijlstra, A. Buursma, and O. W. van Assendelft, Visible and near infrared absorption spectra of human and animal haemoglobin: determination and application (VSP International Science Publ, Utrecht, 2000). OCLC: 248521174.

10. L. M. Coronado, C. T. Nadovich, and C. Spadafora, "Malarial hemozoin: From target to tool," Biochim. Biophys. Acta, Bioenerg. **1840**(6), 2032–2041 (2014).

11. L. H. Miller, "Distribution of Mature Trophozoites and Schizonts of Plasmodium Falciparum in the Organs of Aotus Trivirgatus, the Night Monkey *," The Am. J. Trop. Medicine Hyg. **18**(6), 860–865 (1969).

12. B. Franke-Fayard, J. Fonager, A. Braks, S. M. Khan, and C. J. Janse, "Sequestration and Tissue Accumulation of Human Malaria Parasites: Can We Learn Anything from Rodent Models of Malaria?" PLOS Pathog. **6**(9), e1001032 (2010).

13. K. B. Seydel, D. A. Milner, S. B. Kamiza, M. E. Molyneux, and T. E. Taylor, "The Distribution and Intensity of Parasite Sequestration in Comatose Malawian Children," J. Infect. Dis. **194**(2), 208 (2006).

14. C. Cai, K. A. Carey, D. A. Nedosekin, Y. A. Menyaev, M. Sarimollaoglu, E. I. Galanzha, J. S. Stumhofer, and V. P. Zharov, "In vivo photoacoustic flow cytometry for early malaria diagnosis: Photoacoustic Flow Cytometry for Malaria Diagnosis," Cytom. Part A **89**(6), 531–542 (2016).

15. J. L. Burnett, J. L. Carns, and R. Richards-Kortum, "In vivo microscopy of hemozoin: towards a needle free diagnostic for malaria," Biomed. Opt. Express **6**(9), 3462–3474 (2015).

16. F. Bevilacqua, A. J. Berger, A. E. Cerussi, D. Jakubowski, and B. J. Tromberg, "Broadband absorption spectroscopy in turbid media by combined frequency-domain and steady-state methods," Appl. Opt. **39**(34), 6498–6507 (2000).

17. Q. Fang and D. A. Boas, "Monte Carlo Simulation of Photon Migration in 3D Turbid Media Accelerated by Graphics Processing Units," Opt. Express **17**(22), 20178–20190 (2009). Publisher: Optical Society of America.

18. A. Leproux, T. D. O'Sullivan, A. E. Cerussi, A. Durkin, B. Hill, N. M. Hylton, A. G. Yodh, S. A. Carp, D. A. Boas, S. Jiang, K. D. Paulsen, B. W. Pogue, D. M. Roblyer, W. T. Yang, and B. J. Tromberg, "Performance assessment of diffuse optical spectroscopic imaging instruments in a 2-year multicenter breast cancer trial," J. Biomed. Opt. **22**(12), 121604 (2017).

19. A. Pifferi, A. Torricelli, A. Bassi, P. Taroni, R. Cubeddu, H. Wabnitz, D. Grosenick, M. Möller, R. Macdonald, J. Swartling, T. Svensson, S. Andersson-Engels, R. L. P. v. Veen, H. J. C. M. Sterenborg, J.-M. Tualle, H. L. Nghiem, S. Avrillier, M. Whelan, and H. Stamm, "Performance assessment of photon migration instruments: the MEDPHOT protocol," Appl. Opt. **44**(11), 2104–2114 (2005). Publisher: Optical Society of America.

20. J. B. Fishkin, S. Fantini, M. J. vandeVen, and E. Gratton, "Gigahertz photon density waves in a turbid medium: Theory and experiments," Phys. Rev. E **53**(3), 2307–2319 (1996).

21. A. Kienle and M. S. Patterson, "Improved solutions of the steady-state and the time-resolved diffusion equations for reflectance from a semi-infinite turbid medium," J. Opt. Soc. Am. A **14**(1), 246–254 (1997).

22. H. J. v. Staveren, C. J. M. Moes, J. v. Marie, S. A. Prahl, and M. J. C. v. Gemert, "Light scattering in lntralipid-10% in the wavelength range of 400-1100 nm," Appl. Opt. **30**(31), 4507–4514 (1991).

23. S. H. Chung, A. E. Cerussi, C. Klifa, H. M. Baek, O. Birgul, G. Gulsen, S. I. Merritt, D. Hsiang, and B. J. Tromberg, "In vivowater state measurements in breast cancer using broadband diffuse optical spectroscopy," Phys. Med. Biol. **53**(23), 6713–6727 (2008). Publisher: IOP Publishing.

24. S. H. Chung, A. E. Cerussi, S. I. Merritt, J. Ruth, and B. J. Tromberg, "Non-invasive tissue temperature measurements based on quantitative diffuse optical spectroscopy (DOS) of water," Phys. Med. Biol. **55**(13), 3753–3765 (2010).

25. G. Ganesan, R. V. Warren, A. Leproux, M. Compton, K. Cutler, S. Wittkopp, G. Tran, T. O'Sullivan, S. Malik, P. R. Galassetti, and B. J. Tromberg, "Diffuse optical spectroscopic imaging of subcutaneous adipose tissue metabolic changes during weight loss," Int. J. Obes. **40**(8), 1292–1300 (2016).

26. L. Roland, M. Drillich, and M. Iwersen, "Hematology as a diagnostic tool in bovine medicine," J. VET Diagn. Invest. **26**(5), 592–598 (2014).

27. K. Adeli, J. E. Raizman, Y. Chen, V. Higgins, M. Nieuwesteeg, M. Abdelhaleem, S. L. Wong, and D. Blais, "Complex Biological Profile of Hematologic Markers across Pediatric, Adult, and Geriatric Ages: Establishment of Robust Pediatric and Adult Reference Intervals on the Basis of the Canadian Health Measures Survey," Clin. Chem. **61**(8), 1075–1086 (2015).

28. D. M. Newman, J. Heptinstall, R. J. Matelon, L. Savage, M. L. Wears, J. Beddow, M. Cox, H. D. F. H. Schallig, and P. F. Mens, "A Magneto-Optic Route toward the In Vivo Diagnosis of Malaria: Preliminary Results and Preclinical Trial Data," Biophys. J. **95**(2), 994–1000 (2008).

29. T. Frosch, S. Koncarevic, K. Becker, and J. Popp, "Morphology-sensitive Raman modes of the malaria pigment hemozoin," Analyst **134**(6), 1126–1132 (2009).

30. B. S. Goldschmidt, A. S. M. Sudduth, E. B. Samson, P. Whiteside, K. D. Bhattacharyya, and J. A. Viator, "Total internal reflection photoacoustic spectroscopy for the detection of ?-hematin," J. Biomed. Opt. **17**(6), 061212 (2012).

31. A. Butykai, A. Orbán, V. Kocsis, D. Szaller, S. Bordács, E. Tátrai-Szekeres, L. F. Kiss, A. Bóta, B. G. Vértessy, T. Zelles, and I. Kézsmárki, "Malaria pigment crystals as magnetic micro-rotors: key for high-sensitivity diagnosis," Sci. Rep. **3**(1), 1431 (2013).

32. E. Lukianova-Hleb, S. Bezek, R. Szigeti, A. Khodarev, T. Kelley, A. Hurrell, M. Berba, N. Kumar, U. D'Alessandro, and D. Lapotko, "Transdermal Diagnosis of Malaria Using Vapor Nanobubbles," Emerg. Infect. Dis. **22**(2), 344 (2016).

33. D. J. Cuccia, F. Bevilacqua, A. J. Durkin, F. R. Ayers, and B. J. Tromberg, "Quantitation and mapping of tissue optical properties using modulated imaging," J. Biomed. Opt. **14**(2), 024012 (2009).

34. L. Rénia, S. W. Howland, C. Claser, A. C. Gruner, R. Suwanarusk, T.-H. Teo, B. Russell, and L. F. P. Ng, "Cerebral malaria," Virulence **3**(2), 193–201 (2012). https://doi.org/10.4161/viru.19013.

35. C. Wongsrichanalai, M. J. Barcus, S. Muth, A. Sutamihardja, and W. H. Wernsdorfer, "A Review of Malaria Diagnostic Tools: Microscopy and Rapid Diagnostic Test (RDT)," The Am. J. Trop. Medicine Hyg. **77**(6_Suppl), 119–127 (2007). Publisher: The American Society of Tropical Medicine and Hygiene.

36. A. Trampuz, M. Jereb, I. Muzlovic, and R. M. Prabhu, "Clinical review: Severe malaria," Critical Care **7**(4), 315–323 (2003).

37. T. W. Mwangi, A. Ross, R. W. Snow, and K. Marsh, "Case Definitions of Clinical Malaria under Different Transmission Conditions in Kilifi District, Kenya," J. Infect. Dis. **191**(11), 1932–1939 (2005).